JOURNAL OF THE ROYAL SOCIETY Interface

rsif.royalsocietypublishing.org

Research

Cite this article: Dixon PG, Gibson LJ. 2014 The structure and mechanics of Moso bamboo material. *J. R. Soc. Interface* **11**: 20140321. http://dx.doi.org/10.1098/rsif.2014.0321

Received: 28 March 2014
Accepted: 30 June 2014

Subject Areas:
biomechanics, biomaterials

Keywords:
bamboo, microstructure, mechanical properties, mechanical modelling, cellular solids

Author for correspondence:
L. J. Gibson
e-mail: ljgibson@mit.edu

Royal Society Publishing

The structure and mechanics of Moso bamboo material

P. G. Dixon and L. J. Gibson

Department of Materials Science and Engineering, Massachusetts Institute of Technology, 77 Massachusetts Avenue, 8-032, Cambridge, MA 02139, USA

Although bamboo has been used structurally for millennia, there is currently increasing interest in the development of renewable and sustainable structural bamboo products (SBPs). These SBPs are analogous to wood products such as plywood, oriented strand board and glue-laminated wood. In this study, the properties of natural Moso bamboo (*Phyllostachys pubescens*) are investigated to further enable the processing and design of SBPs. The radial and longitudinal density gradients in bamboo give rise to variations in the mechanical properties. Here, we measure the flexural properties of Moso bamboo in the axial direction, along with the compressive strengths in the axial and transverse directions. Based on the microstructural variations (observed with scanning electron microscopy) and extrapolated solid cell wall properties of bamboo, we develop models, which describe the experimental results well. Compared to common North American construction woods loaded along the axial direction, Moso bamboo is approximately as stiff and substantially stronger, in both flexure and compression but denser. This work contributes to critical knowledge surrounding the microstructure and mechanical properties of bamboo, which are vital to the engineering and design of sustainable SBPs.

1. Introduction

Bamboo has been used as a structural material for millennia. Traditional bamboo structures use entire culms for framing and woven mats for panelling [1,2]. Recently, there has been increasing interest in engineered structural bamboo products (SBPs), analogous to engineered wood products such as plywood and glue-laminated timber [1,2]. The use of SBPs is currently limited by the lack of material property data and appropriate building codes. This study, aimed at increasing the understanding of the structure–property relationships for Moso bamboo, is part of a larger project that includes work on processing of SBPs, on the structural, thermal and moisture performance of SBP, and on life cycle assessment.

Bamboo is an abundant, sustainable resource. According to the FAO's 2010 Forest Resource Assessment, there are 31.4 million hectares of bamboo worldwide, with 60% concentrated in the rapidly developing countries of China, India and Brazil [3]. China is one of the leading producers of bamboo; Moso bamboo (*Phyllostachys pubescens*), the subject of this study, is the most commercially important species in China [4]. Bamboo is ready for harvest in less than 10 years and has a greater yield per hectare and higher strength than traditional timber resources [4,5].

Bamboo belongs to the grass family *Gramineae* (*Poaceae*) [6]. The bamboo macrostructure consists of a generally hollow cylindrical shoot, known as a culm. The culm is divided into sections by nodes that run transversely through the culm cross section; the longitudinal sections between the nodes are known as internodes [7]. In Moso bamboo, the culm diameter and wall thickness decrease with increasing height on the culm [8].

The structure of bamboo is considerably more heterogeneous than that of wood [7]. The majority of bamboo tissue is a composite of vascular bundles embedded in a matrix of parenchyma cells [6]. The vascular bundles consist of hollow vessels surrounded by fibrous sclerenchyma cells [6,7]. The volume fraction of vascular bundles increases radially towards the outer part of the culm [6,7]. A similar, but significantly more gradual, trend is observed along the

height of the culm [6,9]. The volume fraction of solid in the vascular bundles also increases radially towards the outer part of the culm as the vessels become smaller [6]. Both the increasing volume fraction of vascular bundles, and the increasing volume fraction of solid within each vascular bundle lead to a pronounced radial density gradient in the bamboo culm, with denser tissue towards the outer part of the culm. The outer, epidermal layer of bamboo is rather hard, with a waxy surface [1].

This radial density gradient has a profound effect on the mechanical properties of bamboo [8–10]: the axial tensile Young's modulus varies from about 5 to 25 GPa, and the axial tensile strength varies from about 100 to 800 MPa, for specimens taken from the inner and outer culm, respectively [8–10]. The compressive and flexural properties of bamboo along the grain have also been investigated [11–14]; the compressive strength increases with the height on the culm [11,13] and decreasing moisture content [11,14]. For example, Lo *et al*. [13] find the compressive strength of Moso bamboo increases with height along the culm from 45 to 65 MPa, and Lee *et al*. find the flexural strength increases from 70 MPa in the green state to 103 MPa for air-dried bamboo [11]. Most of these investigators probe the mechanical variation with height, and/or some other variable (age, presence of nodes and moisture content). However, very few studies attempt to capture the radial variation of mechanical properties other than tensile properties in the axial direction.

The cell wall structure and mechanical properties have been investigated by X-ray scattering and nanoindentation, respectively. In one study [15], the cellulose microfibrillar angle (MFA) was found to be about 9°, independent of radial and longitudinal position within the culm, while in a second study, the MFA was found to be 10° for the middle and outermost regions, and 44° for the innermost region of bamboo [16]. Nanoindentation of the solid sclerenchyma fibres gave reduced moduli (16.0 GPa) that did not vary significantly with radial position, suggesting that MFA does not vary considerably [15].

Many of the studies that investigate the variation of axial tensile properties across the culm wall, report the properties with respect to fibre volume fraction [8–10]. Linear and rule of mixtures fits are then made of Young's modulus and tensile strength with respect to fibre volume fraction to model the structure, and extrapolate pure fibre properties. Other studies look at the axial properties considering both the microstructure and the macrostructure with analytical and finite-element approaches [7,17], those referenced use gradients found in previous studies.

SBPs are made by cutting the bamboo culm into smaller elements (e.g. strands or wafers) that may be densified by loading them across the grain, prior to bonding them into the final product. The structural performance of the SBP depends, in part, on the variability in the mechanical properties of the elements, both along and across the grain of the culm. While there have been studies on the variation in the tensile properties of bamboo along the grain with radial position, there is little information on the radial variation of the properties across the grain.

In this study, we characterize the microstructure of Moso bamboo quantitatively and measure the axial Young's modulus in bending (or modulus of elasticity, E^*), axial modulus of rupture (in bending) (σ_f^*), axial compressive strength (σ_A^*), radial compressive strength (σ_R^*), and tangential compressive strength (σ_T^*) to assess the effect of the radial density gradient on the mechanical properties of Moso bamboo. In addition, nanoindentation experiments were performed to determine whether there is a gradient in modulus or hardness at the cell wall level. Finally, models relating the structure and mechanical properties were developed and compared with the experimental data.

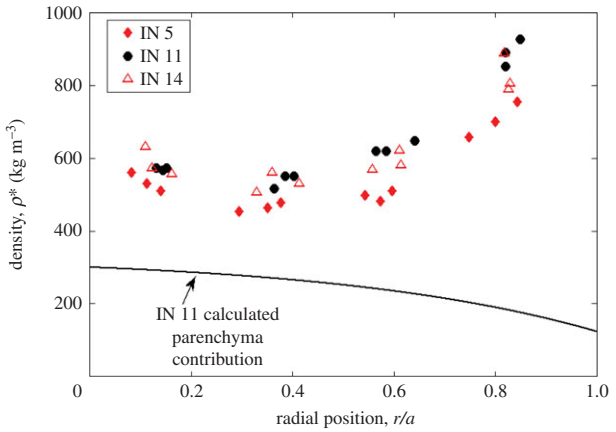

Figure 1. Density plotted against radial position, *r*, normalized by the culm thickness, *a*. (Online version in colour.)

2. Materials

The lower 15 internodes of a dried Moso bamboo culm were obtained from Bamboo Craftsman Company (Portland, OR, USA). The outer diameter of these internodes ranged from 16.8 cm (bottom) to 12.4 cm (top), suitable for structural elements. The diameter at breast height was 13.7 cm, with an average culm wall thickness of 12.0 mm at this height. Internodes were numbered starting at zero, at the base of the culm, and increasing upwards. Specimens from internodes 3 (height from base: 25–40 cm), 5 (50–70 cm), 7 (85–105 cm), 11 (175–205 cm) and 14 (260–290 cm) were characterized in this study. Age of the culm is uncertain.

Specimens were air-dried (moisture content, MC ~ 7%). Moisture content was determined by measuring the mass of three blocks of entire culm wall thickness of the internodes 3, 5, 7, 11 and 14, before and after drying in an oven at 103°C for 24 h. The density of each specimen used for mechanical testing was determined by recording its mass and measuring the specimen dimensions with callipers. The density is plotted against radial position, *r*, in the culm, normalized by the culm wall thickness, *a*, for internodes 5, 11 and 14 in figure 1. The density of the innermost specimens ($r/a < 0.15$) varies between about 500 and 650 kg m^{-3}. The variation stems from the dense inner terminal layer which constitutes more of the specimen volume in the higher internodes, because the culm wall is thinner, making the specimens denser.

3. Microstructure

Uncoated bamboo specimens were imaged using a JOEL JSM-6610LV scanning electron microscope, in low vacuum mode, at a pressure of 30 Pa. Specimens were imaged in both backscatter and secondary modes. Surfaces were prepared by grinding on a Struers Rotopol-1 model polishing wheel with progressively finer silicon carbide papers: 800-grit, 1200-grit, 2400-grit and 4000-grit silicon carbide. Image analysis was performed

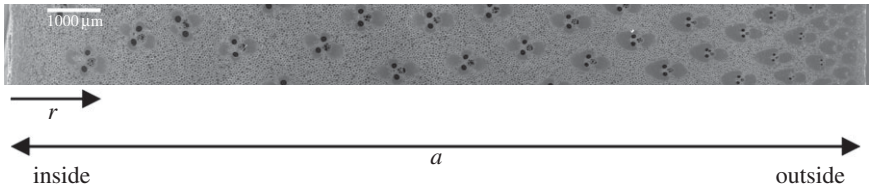

Figure 2. SEM micrograph of Moso bamboo structure, third internode, over entire culm wall thickness.

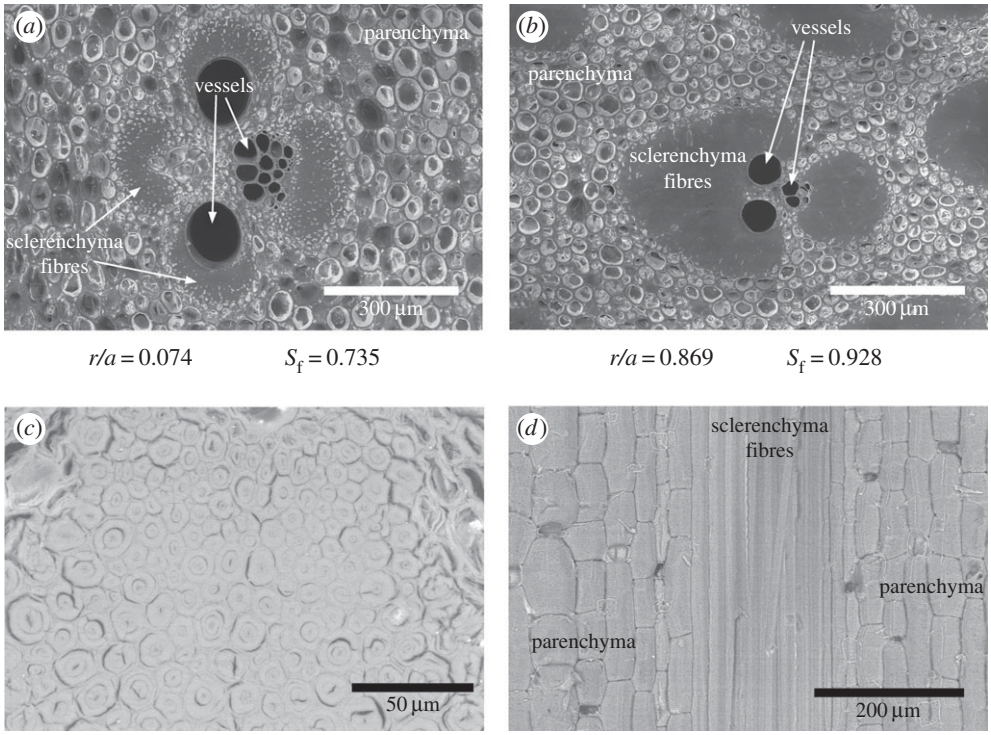

Figure 3. (*a*,*b*) SEM micrographs of inner and outer vascular bundles of internode 7. (*c*) Sclerenchyma fibres, $r/a \sim 0.5$, internode 7. (*d*) Longitudinal section, depicting sclerenchyma fibres (centre) and surrounding parenchyma, $r/a \sim 0.5$, internode 7.

manually using ImageJ, an open-source image analysis software package developed at the National Institutes of Health.

The volume fractions of vascular bundles, V_{vb}, with respect to radial position were measured from individual cross sections of the full culm wall thickness of internodes 3, 5, 7, 11 and 14. The solid fractions of the vascular bundles, S_f, were measured with higher magnification images of individual vascular bundles along the culm wall thicknesses. Intercellular space was approximated as fully solid, namely vessels were considered the only voids of vascular bundles. Parenchyma solid fraction was determined from a total of 13 images of about 30 cells each, from different radial and longitudinal positions in the culm. Areal measurements were used in all cases.

The microstructure of the culm wall, at internode 3, is shown in the scanning electron micrograph of figure 2. The volume fraction of vascular bundles (V_{vb}) increases radially, from the inner to the outer wall. SEM micrographs of individual vascular bundles are shown in figure 3*a*,*b*; similar images were used to measure the solid fraction of the vascular bundles (S_f). These micrographs illustrate the increase in the volume fraction of solid within the vascular bundle, towards the outside of the culm. An SEM micrograph of a cross sectional sclerenchyma fibres within a vascular bundle are shown in figure 3*c*; the fibres are rather solid, with insignificant lumens. A longitudinal section of the sclerenchyma fibres and parenchyma cells is shown in figure 3*d*.

The volume fractions of vascular bundles for four internodes (3, 7, 11 and 14) are plotted as a function of radial position, normalized by total culm wall thickness r/a in figure 4*a*. Best-fit curves, using a constant y-intercept, given below, are also shown as follows:

$$\text{internode 3:} \quad V_{vb} = 0.09 \exp\left(1.654 \frac{r}{a}\right) \quad r^2 = 0.95, \tag{3.1}$$

$$\text{internode 5:} \quad V_{vb} = 0.09 \exp\left(1.640 \frac{r}{a}\right) \quad r^2 = 0.89, \tag{3.2}$$

$$\text{internode 7:} \quad V_{vb} = 0.09 \exp\left(1.834 \frac{r}{a}\right) \quad r^2 = 0.92, \tag{3.3}$$

$$\text{internode 11:} \quad V_{vb} = 0.09 \exp\left(1.938 \frac{r}{a}\right) \quad r^2 = 0.96 \tag{3.4}$$

$$\text{and} \quad \text{internode 14:} \quad V_{vb} = 0.09 \exp\left(2.110 \frac{r}{a}\right) \quad r^2 = 0.98. \tag{3.5}$$

These results are consistent with the nonlinear increase of fibre volume fraction with radial position and the values of fibre fraction found by Nogata and Amada and their coworkers (note: vascular bundle fraction and fibre volume fraction are not the same quantity, but in the plant studied the values are quite similar due to the high solids fraction of the vascular bundles) [8,9].

The general increase in the volume fraction of vascular bundles with radial position gets more pronounced with increasing height on the culm, consistent with the general trend of

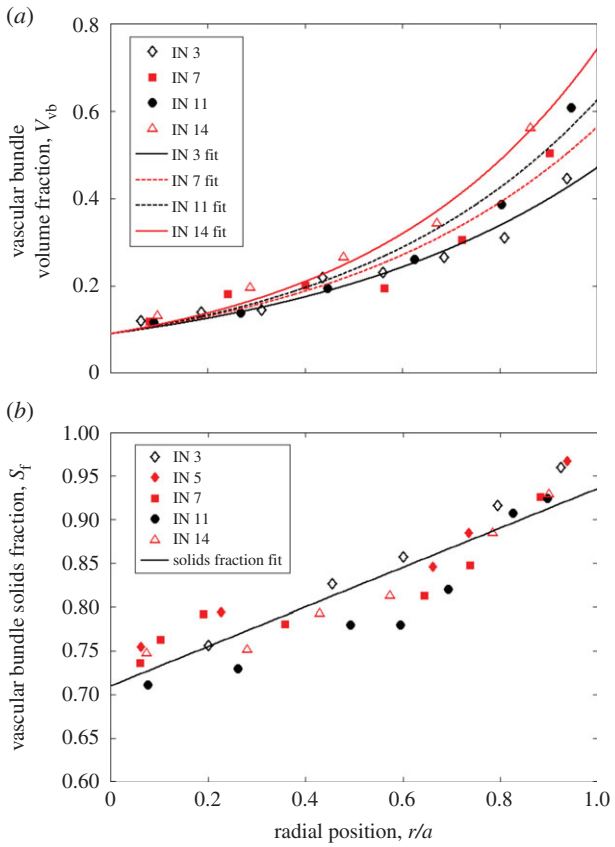

Figure 4. (*a*) Vascular bundle volume fraction plotted against normalized radial position, curves are best-fit equations (3.1), (3.3)–(3.5). (*b*) Vascular bundle solids fraction plotted against normalized radial position, line is best-fit equation (3.6). (Online version in colour.)

increasing fibre fraction with height found by Grosser & Liese [6]. Differences between the various internodes appear slight for the inner portion of the culm. The radial variation is considerably greater than the longitudinal (internode to internode) variation among the internodes studied.

The volume fraction of solid within the vascular bundles is plotted as a function of radial position in figure 4*b*; the data are well described by a linear fit

$$S_f\left(\frac{r}{a}\right) = 0.226 \cdot \left(\frac{r}{a}\right) + 0.710 \quad r^2 = 0.84. \tag{3.6}$$

The vascular bundles' solid fraction increases with radial position, but not with height in the culm. The vessels clearly shrink from the inside to the periphery of the culm wall (figures 2 and 3*a*,*b*). The vascular bundles also show a change in shape with radial position. The inner and middle bundles show four distinct sclerenchyma fibre areas surrounding the vessels and appear clover shaped. The outer vascular bundles show two surrounding sclerenchyma regions and appear skull shaped. These changes are not considered in subsequent analysis.

The average of relative density (or solid fraction) of the parenchyma was found to be 0.22 ± 0.03, and while the parenchyma lumen size does tend to be smaller in the outermost regions of the culm, a constant value of solid fraction of the parenchyma was used for simplicity. For internode 3, the relative density of the parenchyma tissue ranged from 0.23 to 0.26, from the inner to the outer region, whereas for internode 7, it ranged from 0.18 to 0.21. Assuming that the density of the solid cell wall material is similar to that for wood ($1500\ \mathrm{kg\ m^{-3}}$ [18–20]), the average density of the

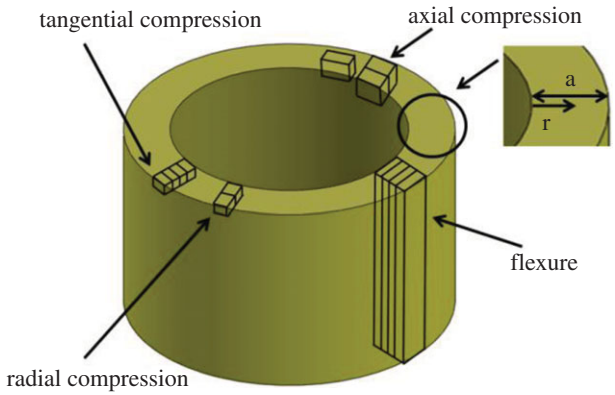

Figure 5. Geometry of mechanical test specimens. (Online version in colour.)

parenchyma cells is $330\ \mathrm{kg\ m^{-3}}$. The contribution of the parenchyma to the overall density, as a function of radial position, can then obtained by multiplying this value times the volume fraction of parenchyma $V_p = 1 - V_{vb}$; this is shown on figure 1, for internode 11. The aspect ratio of the elongated brick-like parenchyma cells was 1.9 ± 0.4, measured from axial-tangential cross sections of internodes 3, 7 and 11, similar to figure 3*d*.

4. Mechanical test methods

4.1. Flexure tests

Small axial bending specimens were cut at different radial positions within the culm wall thickness from internodes 5, 11 and 14 to determine the radial variation of flexural properties. The waxy epidermal layer was removed and four strips were cut by splitting. Beams were then manually cut and sanded from these strips. The beams had the following nominal dimensions: length, 100–130 mm (along the axial direction); width, 6–12 mm (along the tangential direction); and thickness, 1–4 mm (along the radial direction). The span to depth ratio was no less than 20 for each specimen (figure 5). Specimen density was measured. Three sets of specimens were taken from each internode, giving a total of 36 specimens tested in flexure. Beams were tested with outer surfaces face up, at a crosshead speed of $1\ \mathrm{mm\ min^{-1}}$, in three-point bending. The deflection at the centre of the beam was measured with a linear variable differential transducer, and the load was measured with a 500 N load cell.

4.2. Compression tests

Compression tests were performed in the axial, radial and tangential directions on rectangular prismatic specimens that were cut from the bulk and minimally planed and sanded to achieve a rectangular cross section. For testing in the axial direction, rectangular prisms were fabricated from internodes 3, 7 and 11. Rectangular blocks from the entire culm thickness were split in the middle to create an inner and outer piece giving a nominal thickness : width : height ratio of 1 : 2 : 2, and in the neighbouring regions, specimens were cut from the middle of the blocks with the same geometry. The aspect ratio was chosen to avoid failure by macro-buckling and obtain crushing strength values. Specimen dimensions were from 5 to 7 mm (along the radial direction): 10 to 14 mm (along the tangential direction): 10 to 14 mm (along the axial direction) (figure 5). At least three tests were performed

using specimens at each of the various radial positions and heights. The crosshead speed was 0.5 mm min^{-1}. Displacement was measured either using a linear variable differential transducer measuring the displacement between the compression plates or the crosshead displacement directly from the Instron; a comparison of the two methods on individual specimens gave similar results. Load was measured with a 45 kN load cell. Thirty-six axial compression tests were performed in total.

Specimens for testing in compression in the radial direction were prepared from internodes 3, 7 and 14. Rectangular pieces were cut from the entire culm wall thickness. These specimens were then split longitudinally in the middle. Specimens had a nominal thickness : width : height ratio of 1 : 1 : 2. Specimen dimensions were from 2.5 to 4 mm (along the axial direction): 2.5 to 4 mm (along the tangential direction): 5 to 8 mm (along the radial direction) (figure 5). A set of at least three tests was done using each of these types of specimens. Displacement between the compression plates was measured with a linear variable differential transducer; the crosshead speed was 0.3 mm min^{-1}. Load was measured with a 500 N load cell. Twenty-one radial compression tests were performed in total.

Tangential compressive strength specimens were prepared from internodes 3 and 7. The entire wall thickness was split into four blocks with the dimension parallel to tangential being the largest. In the case of internode 3, the inner terminal layer and the cortex were removed, whereas in internode 7 these regions were left on the innermost and outermost specimens. Specimen dimensions were from 3 to 4 mm (along the radial direction): 3 to 4 mm (along the axial direction): 6 to 8 mm (along the tangential direction) (figure 5). The load was measured with a 5 kN load cell, and the displacement was measured with the crosshead displacement or a linear variable differential transducer.

Radial compression tests were also performed in a deformation stage within the SEM (Deßen Microtest 200 N Tensile Tester). Specimens of similar geometry to those used in the Instron tests were used. Uncoated and gold-coated specimens were tested. The load was measured with a 200 N load cell and the displacement was measured using the stepper motor that drove the crosshead. The test speed was 0.1 mm min^{-1}. The crosshead was stopped at several points during the loading, to obtain images of the deformation. It was not possible to do axial compression tests in the deformation stage, as the specimen dimensions would have to be unreasonably small to fail using the 200 N load cell.

4.3. Nanoindentation

Nanoindentation was performed on the sclerenchyma fibre bundles using a Hysitron TriboIndenter with a Berkovich tip, and a dynamic mechanical analysis transducer. A trapezoidal loading profile with a peak load of 500 µN, 10 s hold and 5 s ramps was used. Five by five grid patterns with 25 µm separation were used, for a total of 25 indents on each fibre bundle indented. Nanoindentation was performed on internodes 3, 7 and 14. For each internode, 25 indents were made on fibres at three different radial positions: inner, middle and outer (approx., $r/a = 0.25$, 0.50 and 0.75, respectively). Oliver-Pharr analysis of the unloading curve was used for the determination of reduced moduli [21]. The raw data suggested that the reduced modulus and hardness showed little positional effects, in either the radial or longitudinal direction. Indents were filtered for outliers using the interquartile range (IQR) of the effective depth computed from all the indents. The effective depths outside the 1.5 × IQR of the median were removed, leaving 191 indents out of a total of 225.

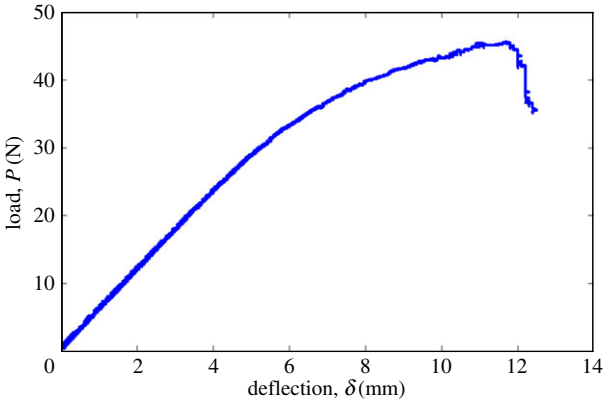

Figure 6. Typical load–deflection curve for a bending test (specimen: internode 14, $r/a = 0.817$, $\rho^* = 888$ kg m^{-3}, width = 6.85 mm; thickness = 1.90 mm; span length = 85.73 mm). (Online version in colour.)

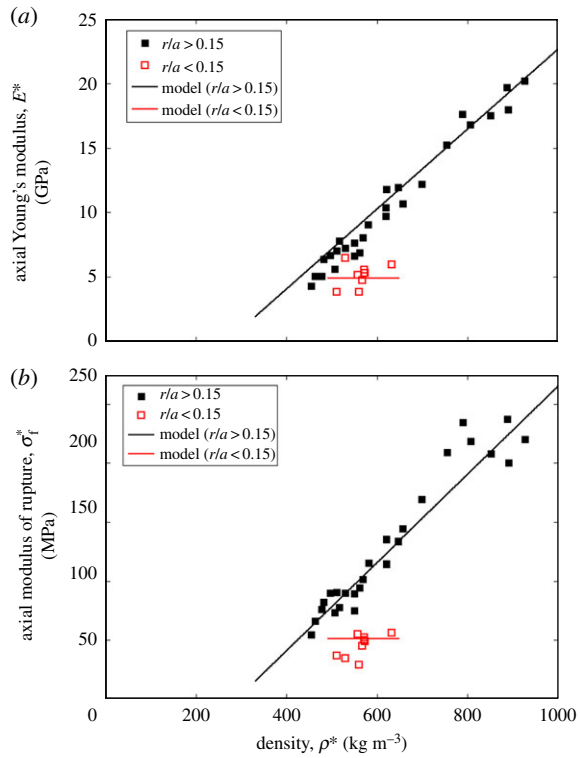

Figure 7. (*a*) Young's modulus along the axial direction from bending plotted against density, lines represent the model. (*b*) Modulus of rupture along the axial direction plotted against density, lines represent the model. (Online version in colour.)

5. Mechanical test results

A typical load-deflection curve for a bending test is shown in figure 6. Ultimate failure always occurred on the tensile side of the beams. The flexural Young's modulus, E^*, and modulus of rupture, σ_f^*, are plotted against density in figure 7. For the specimens at $r/a > 0.15$, both Young's modulus and modulus

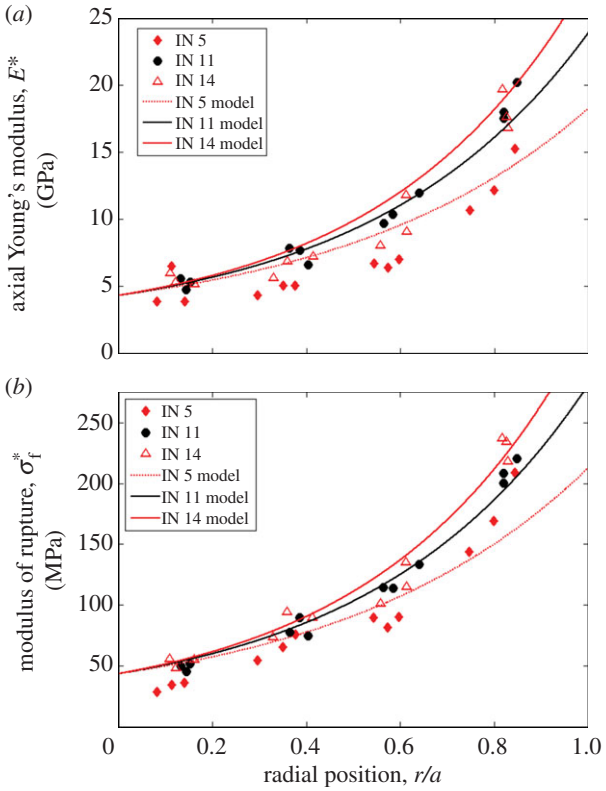

Figure 8. (*a*) Young's modulus along the axial direction from bending plotted against normalized radial position, curves represent the model. (*b*) Modulus of rupture along the axial direction plotted against normalized radial position, curves represent the models. (Online version in colour.)

of rupture increase linearly with density. The best linear fit to the flexural Young's modulus data for these specimens is

$$E^* = 1.27E_s\left(\frac{\rho^*}{\rho_s}\right) - 10.59 \quad [n = 27, r^2 = 0.97], \qquad (5.1)$$

with E^* in GPa. The best linear fit to the modulus of rupture data for these specimens is

$$\sigma_f^* = 1.25\sigma_{fs}\left(\frac{\rho^*}{\rho_s}\right) - 117.5 \quad [n = 27, r^2 = 0.93], \qquad (5.2)$$

with σ_f^* in MPa. Extrapolation of ρ^* to the fully dense value for the cell wall, $\rho_s = 1500\ \mathrm{kg\ m^{-3}}$, gives estimates for Young's modulus, E_s, and modulus of rupture, σ_{fs}, of the solid cell wall material on the axial direction: $E_s = 39.8$ GPa and $\sigma_{fs} = 472$ MPa. For the innermost specimens, at $r/a = 0.08$–0.15, Young's modulus and modulus of rupture are nearly constant. Young's modulus and modulus of rupture data are replotted against radial position within the culm, r/a, in figure 8. The lines in figure 7 and the curves in figure 8, representing models for the flexural Young's modulus and modulus of rupture, are described in the following section.

Typical compressive stress–strain curves are shown in figure 9. Compressive strengths for loading in the axial, radial and tangential directions are plotted against density in figure 10. The axial compressive strength, σ_A, increases linearly with density, ρ^*; the best linear fit to the data is

$$\sigma_A^* = 1.20\sigma_s\left(\frac{\rho^*}{\rho_s}\right) - 49.69 \quad [n = 36, r^2 = 0.95], \qquad (5.3)$$

with σ_A^* in MPa. Extrapolation to the fully dense value for the cell wall, at $\rho_s = 1500\ \mathrm{kg\ m^{-3}}$, gives an estimate for the compressive strength of the solid cell wall material, $\sigma_s = 248$ MPa.

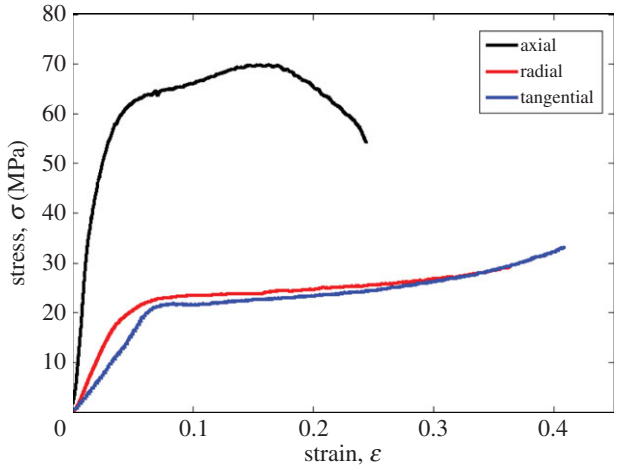

Figure 9. Typical axial compression stress–strain curve (axial specimen: internode 11, $r/a = 0.444$, $\rho^* = 541\ \mathrm{kg\ m^{-3}}$, radial specimen: internode 7, $r/a = 0.259$, $\rho^* = 585\ \mathrm{kg\ m^{-3}}$, tangential specimen: internode 7, $r/a = 0.357$, $\rho^* = 556\ \mathrm{kg\ m^{-3}}$). (Online version in colour.)

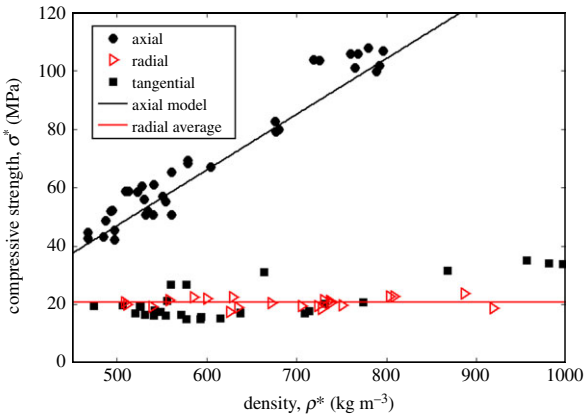

Figure 10. Compressive strength in the axial, radial and tangential directions, plotted against density, upper line represents the model and lower line is radial strength average. (Online version in colour.)

By contrast, the radial strength is roughly constant at about 20 MPa, independent of density. The compressive strength in the tangential direction is similar to that in the radial direction, with the exception of the outermost and innermost specimens of internode 7, which included, respectively, the hard outer cortex and the inner terminal layer, with thick-walled parenchyma cells elongated on the tangential direction. The dense epidermal layer and terminal layer bear higher stresses when loaded in the tangential direction than in the radial direction. The lines on figure 10 represent the axial model, described in the following section, and the radial average.

The axial compressive data, plotted against normalized radial position, r/a, within the culm, for each internode (3, 7 and 11), are shown in figure 11; the curves, representing models for the compressive strengths, are described in the following section.

Deformation stage tests in the SEM indicate that in radial compression, the bamboo fails by collapse of the vessels in the vascular bundles (figures 12 and 13). We note that the higher magnification images in figure 13 clearly show the vascular bundles collapsing, with little deformation visible in the parenchyma tissue.

The average reduced modulus and hardness, from nanoindentation of the solid cell wall in the sclerenchyma fibres,

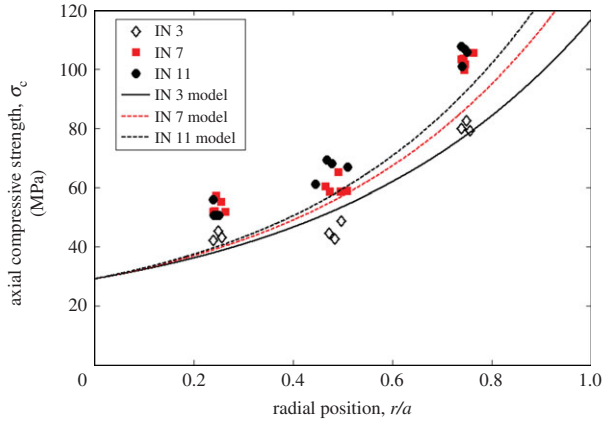

Figure 11. Compressive strength in the axial direction plotted against normalized radial position, curves represent the models. (Online version in colour.)

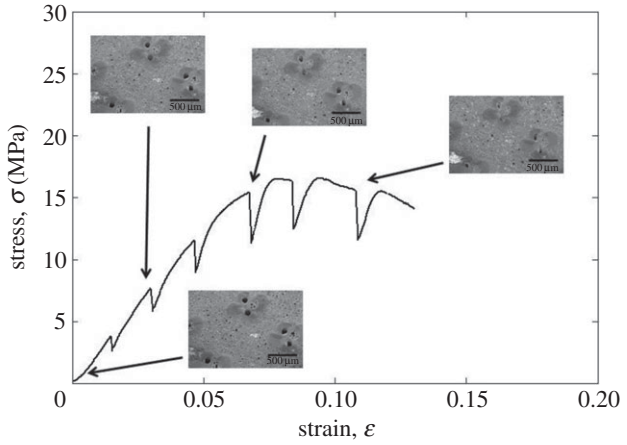

Figure 12. Stress–strain curve from deformation stage test, with micrographs of the specimen superimposed on the curve with arrows indicating stress for each image.

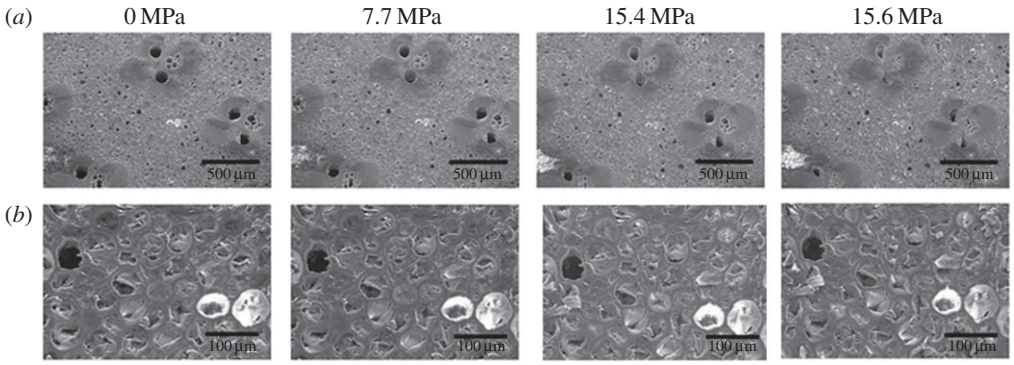

Figure 13. Micrographs of gold-coated internode 7 specimen under compressive loading in the radial direction, with radial stress shown above each image. (*a*) The composite structure, same as images in figure 12. (*b*) The higher magnification micrographs of the same location showing only the parenchyma under loading.

are 14.9 ± 2.3 GPa and 289 ± 64 MPa (table 1), respectively, similar to literature values of 16.0 ± 3.15 GPa and 360 ± 104 MPa for Moso bamboo (values given as average ± s.d.) [15]. While there are slightly different values with varying radial and longitudinal positions, all values of both reduced modulus and hardness were within 1 s.d. of the mean, suggesting that the sclerenchyma fibre properties are roughly constant within the culm. The mean reduced modulus value, 14.9 GPa, is significantly lower than the axial Young's modulus of the solid cell wall, 39.8 GPa, extrapolated from flexural tests at the density of the solid cell wall ($\rho_s = 1500$ kg m^{-3}). The reduced modulus obtained from nanoindentation is also significantly lower than the axial Young's modulus of the densest specimens (20 GPa). This underestimation is due to anisotropy in the cell wall; contact experiments, by their design, measure a combination of the transverse and axial properties. The reduced modulus of wood cell wall has been found to depend on the anisotropic elastic constants [22,23]. The transverse fibre Young's modulus of bamboo is likely substantially less than the axial value, as is the case in wood, where, for example, the transverse and axial moduli for the solid cell wall are 10 and 35 GPa, respectively [24].

6. Modelling

The structure of Moso bamboo can be modelled as a fibre composite, with the vascular bundles acting as the fibre and the parenchyma as the matrix. In this model, we assume that the properties of the solid in both the vascular bundles and the parenchyma are the same.

6.1. Young's modulus

Young's modulus of the bamboo, E_A^*, in the axial direction is then

$$E_A^* = E_p V_p + E_{vb} V_{vb}, \tag{6.1}$$

where E_p and E_{vb} are Young's moduli of the parenchyma and vascular bundles, respectively, and V_p and V_{vb} are their respective volume fractions.

The parenchyma cells are roughly aligned, but have substantial curvature in many of the cell walls and are relatively equiaxed compared with fibres: they resemble a closed cell foam with curved cell walls (figure 3). Previous studies on closed-cell aluminium foams with curved cell walls have found that they behave mechanically like open-cell foams: the modulus varies with relative density squared and the compressive strength varies with relative density raised to the 3/2 power; these relationships describe the modulus and strength up to relative densities of 0.3 [25]. Our estimate of Young's modulus of the parenchyma is

$$E_p = \left(\frac{\rho^*}{\rho_s}\right)_p^2 E_s, \tag{6.2}$$

where E_s is Young's modulus of the solid cell wall material.

Table 1. Reduced modulus and hardness from nanoindentation tests. Note: mean ± s.d.; (*n*) is the number of indentations.

	internode number		
radial position	3	7	14
reduced modulus (GPa)			
$r/a \sim 0.25$	13.9 ± 2.49 (14)	16.08 ± 1.89 (23)	13.52 ± 1.79 (23)
$r/a \sim 0.50$	12.93 ± 2.27 (14)	16.04 ± 2.29 (25)	14.04 ± 1.65 (21)
$r/a \sim 0.75$	15.2 ± 1.29 (24)	16.72 ± 2.30 (24)	14.11 ± 1.38 (23)
internode average	14.24 ± 2.14 (52)	16.28 ± 2.17 (72)	13.88 ± 1.61 (67)
combined average	14.88 ± 2.26		
hardness (MPa)			
$r/a \sim 0.25$	266.2 ± 87.5 (14)	296.5 ± 54.5 (23)	249.4 ± 48.8 (23)
$r/a \sim 0.50$	255.1 ± 75.6 (14)	310.3 ± 59.5 (25)	258.0 ± 47.3 (21)
$r/a \sim 0.75$	301.6 ± 42.5 (24)	346.0 ± 69.7 (24)	284.8 ± 34.4 (23)
internode average	279.6 ± 68.3 (52)	317.8 ± 64.2 (72)	264.2 ± 45.9 (67)
combined average	288.6 ± 63.9		

The relative density of the parenchyma $(\rho^*/\rho_s)_p$ is roughly constant, at 0.22, throughout the Moso bamboo culm. We assume that the solid cell wall moduli of the parenchyma and the fibres are the same. Taking $E_s = 39.8$ GPa, extrapolated from our bending tests, E_p is 1.93 GPa. Young's modulus of the vascular bundles can be estimated from the solid fraction of the bundles, S_f (figure 4*b*), and the solid cell wall modulus, $E_s = 39.8$ GPa, so that

$$E_A^* = E_p(1 - V_{vb}) + S_f E_s V_{vb}. \quad (6.3)$$

The dependence of the axial modulus with density can then be found given the dependence of the vascular bundle volume fraction, V_{vb}, and solids fraction, S_f, on radial and internode number (longitudinal position) (figure 4) and the radial position and density of each of the flexural specimens. For each of the flexural test specimens, for $r/a > 0.15$, the vascular bundle volume fraction and solids fraction were calculated based on each specimen's radial position and internode number using the best-fit curves to the data in figure 4 (equations (3.1)–(3.6)). The calculated values of V_{vb} and $V_{vb}S_f$ are plotted against specimen density, ρ^* in figure 14. At zero volume fraction of vascular bundles, the tissue is entirely parenchyma, with an average density equal to the relative density of the parenchyma times the solid cell wall density; using $(\rho^*/\rho_s)_p = 0.22$ and $\rho_s = 1500$ kg m^{-3}, the parenchyma density is 330 kg m^{-3}. Linear equations were then fit to the calculated values for the V_{vb} and $V_{vb}S_f$ as functions of density, with zero volume fraction of vascular bundles (i.e. all parenchyma) fixed to a density of 330 kg m^{-3} (equations (6.4)–(6.5))

$$V_{vb}S_f = 0.000825\rho* - 0.27228 \quad r^2 = 0.86 \quad (6.4)$$

$$\text{and} \quad V_{vb} = 0.000945\rho* - 0.31172 \quad r^2 = 0.80. \quad (6.5)$$

The linear fits are also shown in figure 14. Substituting equations (6.4) and (6.5) into equation (6.3) then gives the dependence of the axial Young's modulus on density.

The model is plotted along with the data for the specimens with $r/a > 0.15$ in figure 7*a*; it overpredicts the modulus slightly at lower densities and gives a good description of the data at higher densities. The model is valid for densities above 330 kg m^{-3}, corresponding to all parenchyma tissue. The lowest measured density of the flexural specimens was roughly 460 kg m^{-3}, which occurred at $r/a \sim 0.30$ in internode 5. The lowest density occurs in the second innermost position due to the terminal layer on the innermost specimens. At this density, the tissue is estimated to have roughly 88% parenchyma and 12% vascular bundles.

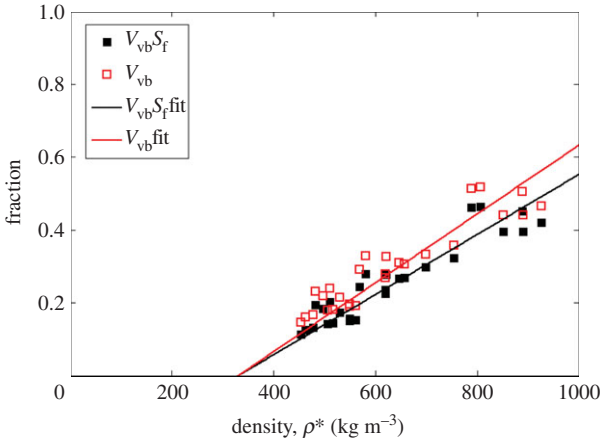

Figure 14. Calculated fractions of V_{vb} and $V_{vb}S_f$ of outer flexural specimens plotted against measured density, lines are best-fit equations (6.4) and (6.5). (Online version in colour.)

The modulus of the 'innermost' tissue represented in figure 7*a*, at $r/a < 0.15$, is roughly constant at 5.13 GPa. The density of these specimens varies between about 500 and 650 kg m^{-3}. For $r/a = 0.10$, the volume fraction of vascular bundles, $V_{vb} = 0.11$ and the solid fraction within the bundles is about 0.73; the corresponding theoretical density is 450 kg m^{-3}; the somewhat higher density of the innermost specimens and their variation in density is due to the dense terminal layer. Substituting $V_{vb} = 0.11$ and $S_f = 0.73$ values in equation (6.3) gives $E^* = 4.91$ GPa, similar to the measured values. The terminal layer region constitutes more of the specimen volume in the higher internodes, because the culm wall is thinner. The cells in the dense terminal layer are oriented with

their prism axis in the tangential direction [26], so that in the bending tests, they are relatively compliant.

This model can also be applied to the variation in Young's modulus with radial and internode position (figure 8*a*), using the best-fit curves for the volume fraction of vascular bundles, V_{vb}, and the solid fraction within the vascular bundles, S_f, as a function of the radial position, r/a (figure 4, equations (3.1)–(3.6)). The model gives a good description of the results for internodes 11 and 14, but overpredicts the data for internode 5.

6.2. Modulus of rupture

The modulus of rupture of bamboo, for loading in the axial direction, can be estimated using the rule of mixtures:

$$\sigma_f^* = 0.3\left(\frac{\rho^*}{\rho_s}\right)_p^{3/2}\sigma_{fs}(1 - V_{vb}) + S_f V_{vb}\sigma_{fs}, \qquad (6.6)$$

where σ_{fs} is the modulus of rupture of the solid cell wall material, estimated by extrapolating the bending strength results to a relative density of 1 ($\sigma_{fs} = 472$ MPa). The rule of mixtures for the strength is a simplification of composites failure, but often predicts experimental results well [27,28]. The first term models the parenchyma contribution as that of an open-cell foam [18], similar to previous results on closed-cell aluminium foams with curved cell walls [25]; for the constant relative density of 0.22 of the parenchyma, its modulus of rupture is 14.6 MPa. The second term gives the vascular bundle contribution. The dependence of the modulus of rupture of bamboo on density can then be obtained using equations (6.4) and (6.5). The model is shown in figure 7*b*; it gives a good description of the modulus of rupture of the bamboo for the specimens with $r/a > 0.15$. As for Young's modulus, the model is valid for densities greater than 330 kg m^{-3}.

The modulus of rupture of the 'innermost' tissue represented in figure 7*b*, at $r/a < 0.15$, is roughly constant at 45.0 MPa. For normalized radial position, $r/a = 0.10$, the volume fraction of vascular bundles, $V_{vb} = 0.11$ and the solid fraction within the bundles is about 0.73; the corresponding theoretical density is 450 kg m^{-3}. Substituting $V_{vb} = 0.11$ and $S_f = 0.73$ values in equation (6.6) gives $\sigma_f^* = 50.9$ MPa, similar to the measured values. The contribution of the terminal layer to the modulus of rupture is small, for the same reasons as for Young's modulus.

The model can also be applied to the variation in the modulus of rupture with radial position (figure 8*b*), using the best-fit curves for the volume fraction of vascular bundles, V_{vb}, and the solid fraction within the vascular bundles, S_f, as a function of the radial position, r/a (figure 4, equations ((3.1)–(3.6)). The model gives a good description of the data.

6.3. Axial compressive strength

The compressive strength in the axial direction is modelled in a similar way

$$\sigma_A^* = 0.3\left(\frac{\rho^*}{\rho_s}\right)_P^{3/2}\sigma_{fs}(1 - V_{vb}) + S_f V_{vb}\sigma_s, \qquad (6.7)$$

where σ_s is the compressive strength, in the axial direction, of the solid cell wall material, extrapolated from the compression test results at a relative density of 1 ($\sigma_s = 248$ MPa). In equation (6.7), the strength of the parenchyma is modelled assuming cell wall bending and failure by plastic hinges [18]. Thus, the solid cell wall modulus of rupture ($\sigma_{fs} = 472$ MPa) is used. Substituting equations (6.4) and (6.5) into equation (6.7) gives the model for the axial compressive strength in terms of density. The solid black line on figure 10 corresponds to the model; it predicts the compressive strength over the range of densities of bamboo tested fairly well. The model is valid for densities over 330 kg m^{-3}, corresponding to all parenchyma.

This model can also be applied to the variation in the compressive strength in the axial direction with radial and internode position (figure 11), using the best-fit curves for the volume fraction of vascular bundles, V_{vb}, and the solid fraction within the vascular bundles, S_f, as a function of the radial position, r/a (figure 4, equations ((3.1)–(3.6)). The model follows the same trend as the data, but somewhat underpredicts it.

6.4. Transverse compressive strength

The transverse compressive strength showed little density dependence, except at the highest densities, for which the terminal layer or epidermal layer increased the strength. The overall lack of density dependence is not surprising, considering that the transverse compressive strength of fibre-reinforced composites is thought to be independent of fibre volume fraction [29]. However, deformation stage results (figures 12 and 13) suggest transverse compressive failure occurs by crushing of the vessels in the vascular bundles. We note that the volume fraction of vessels, $V_{vb}(1 - S_f)$, is roughly constant with radial position, r/a and with density, consistent with the roughly constant transverse compressive strength.

7. Discussion

Moso bamboo has both a radial and longitudinal density gradient as a result of the variation in the volume fraction and solids fraction of the vascular bundles (figures 2 and 4). We have used our measurements of the vascular bundle volume fraction and solids fraction and the overall density to develop models for the mechanical properties of bamboo based on both density and radial position.

The flexural modulus and strength in the axial direction, of all but the innermost specimens at $r/a < 0.15$, increase linearly with density, demonstrating the same general trend as wood [18]. The axial flexural Young's modulus varies from about 5 to 20 GPa (figures 7*a* and 8*a*), in good agreement with data for tensile moduli from the literature [9,10]. The modulus of rupture has a range from 50 to 250 MPa, slightly lower than the range of the majority of literature for tensile strength (100–400 MPa) [8–10]. The variation of these flexural properties with density is similar to that found by Li [30].

The extrapolated Young's modulus of the solid cell wall, $E_s = 39.8$ GPa is similar to values extrapolated from tensile tests by Shao *et al.* (40 GPa) and lower than that found by Amada *et al.* (46 GPa) and Nogata *et al.* (55 GPa) [8–10]. The extrapolated modulus of rupture of the cell wall, $\sigma_{fs} =$ 472 MPa, is lower than extrapolated tensile strengths (580–810 MPa) [8–10]. These results suggest that the modulus of rupture is a conservative estimate of tensile strength, much like modulus of rupture for clear wood [31].

The model for Young's modulus in the axial direction somewhat overpredicts the data at low densities and radial positions (figures 7*a* and 8*a*). We have assumed that Young's modulus of the solid cell wall is the same for the

Table 2. Comparisons of Moso bamboo and North American wood properties [31]. Note: wood properties at 12% moisture content. Moso bamboo average density, Young's modulus and modulus of rupture are those of flexure specimens for $r/a > 0.15$. Moso average axial compressive strength is from all axial compression specimens.

material	density (kg m^{-3})	axial compressive strength (MPa)	Young's modulus (GPa)	modulus of rupture (MPa)
Moso bamboo	630	69.1	10.56	130.0
eastern white pine	350	33.1	8.50	59.0
Douglas fir, coast	480	49.9	13.40	85.0
white spruce	360	35.7	9.60	65.0
northern red oak	630	46.6	12.50	99.0

parenchyma and sclerenchyma (equation (6.3)); this likely causes an overestimation of the parenchyma's role in axial elasticity, which manifests at higher fractions of parenchyma, corresponding to lower densities and radial positions. Despite the overprediction, the modelled Young's modulus captures the general range and variation of the experimental values. The model for the modulus of rupture in the axial direction predicts the experimental values well (figures 7*b* and 8*b*), suggesting that the parenchyma strength is not overpredicted in equation (6.5), and that the parenchyma contributes to the flexural strength of bamboo.

The innermost specimens, at $r/a < 0.15$, show relatively constant Young's modulus and modulus of rupture with density. For $r/a < 0.15$, the volume fraction of vascular bundles and their solid fraction are about constant; the variation in density, between about 500 and 650 kg m^{-3}, largely arises from the dense terminal layer. The model, using the value for the vascular bundle volume fraction and solid fraction at $r/a = 0.10$, gives a good estimate of Young's modulus of the innermost specimens. The innermost specimens also have a roughly constant value of modulus of rupture, for the same reason.

The compressive strength of Moso bamboo in the axial direction increases linearly with density, from 40 to 110 MPa (figure 10), similar to the trend of flexural properties of bamboo and to that of wood [18]. Literature values, from 45 to 65 MPa, have been obtained on tests on short longitudinal specimens of the entire culm [13], which include both low- and high-density regions of the culm. Additional factors, such as moisture content, specimen size, aspect ratio may also contribute to the difference in the data. The moisture content for the specimens in this study is about 7%, while that for a previous study is about 12% [13]. Moso bamboo shows a steep decrease in its compressive strength with increasing moisture content [14], similar to wood [32]. The model for the compressive strength predicts the experimental values well (figures 10 and 11). The radial and tangential compressive strengths of Moso bamboo are roughly constant with density (figure 10). Deformation stage results suggest that transverse compressive failure occurs by crushing of the vessels of vascular bundles (figures 12 and 13), consistent with the roughly constant volume fraction of vessels. It was somewhat surprising that the parenchyma did not fail in transverse loading, but there was little indication of this failure mechanism.

The axial properties of Moso bamboo scale linearly with density, similar to wood as previously mentioned. However, in the case of bamboo, relationships between the axial properties (Young's modulus, modulus of rupture and compressive strength) and density are not proportional as is the case with wood [18]. This deviation from proportionality arises from the composite-like structure of bamboo, consisting mainly of sclerenchyma fibres and parenchyma each of different relative densities. The wood structure resembles a honeycomb, in which the density variation is due to differences in the fibre cell wall thickness relative to the fibre cell size [18,33]. In bamboo, the density variation is due to different proportions of the constituents. Our model accounts for the variation in the fractions of parenchyma and vascular bundles and applies simple cellular material models to these constituents. In the model, cell wall properties of both the fibres and the parenchyma are assumed to be the same and are obtained from fits of the data (equations (5.1)–(5.3)) extrapolated to the density of the solid cell wall ($\rho_s = 1500$ kg m^{-3}).

Flexure was investigated due to its importance for structures. Unfortunately, the modulus of rupture is not a fundamental materials strength property, as flexural strength is governed by both tensile and compressive behaviour, and is calculated assuming linear elasticity [34]. This fact complicates the extrapolation of the solid cell wall modulus of rupture, σ_{fs} and subsequent modelling. The extrapolation and modelling of modulus of rupture tacitly assumes the property behaves like tensile strength. For wood, the modulus of rupture is a conservative estimate of tensile strength and considered a quality material property for beams of different sizes and species [31,34]. Based on the tensile results of others [8–10], this appears to be the case for Moso bamboo justifying the model to an extent. The model's good agreement with the experimental data provides some verification of this assumption.

The mechanical properties of Moso bamboo can be compared to North American softwoods commonly used for structural purposes (table 2), such as eastern white pine, Douglas fir and white spruce. Young's modulus is comparable (except for Douglas fir, which is higher than Moso bamboo), while the modulus of rupture and compressive strength of the bamboo are much higher than the above softwoods; the average density of Moso bamboo is significantly higher than all of these softwoods [31]. Comparison of transverse data is unclear, as most transverse data on wood is performed using a practical engineering test that has some indentation character [35].

It is important to note that the average density of the Moso bamboo studied is significantly higher than that of any of these softwoods and is similar to that of northern red oak, a commercially important North American hardwood. Our data for Moso bamboo indicates that it is 31% stronger in bending, 15% less stiff and 48% stronger in compression than red oak [31]. It is worth noting that while the compressive strength

results are impressive, Young's modulus determined from bending tests is comparatively low when compared with wood, suggesting that structural Moso bamboo members in compression could be limited by buckling. Also it should be noted the wood properties were determined with larger specimens of higher moisture content.

8. Conclusion

The Moso bamboo structure is clearly graded, and the volume fraction of vascular bundles is significantly higher in the outer regions of the culm wall. In addition to bamboo's vascular bundle volume fraction increasing radially, their solid fraction increases radially as well. Nanoindentation results suggest the fibres' properties do not vary greatly with position in the culm.

The mechanical properties show significant variation with radial position. Axial properties increase linearly with density, while the transverse compressive strength shows little variation. Compared with North American softwoods, Moso bamboo is stronger, approximately as stiff, but significantly denser. From this study, stiffness and weight requirements would seem to be a possible limiting factor in the design and use of Moso bamboo. Additionally, the density and strength would likely present difficulties in the processing of Moso bamboo; traditional wood processing techniques would likely need to be modified to account for this as well as bamboo's tubular geometry.

Moso bamboo can be modelled as a fibre-reinforced composite, with a parenchyma matrix and vascular bundle fibres as a first approximation. The experimental Young's modulus and models created from images suggest that the sclerenchyma fibres dominate axial elasticity. The relatively good agreement of models of axial strengths (modulus of rupture and compressive strength) with experimental data suggests there is a significant contribution from the parenchyma, which can be approximated as a foam with solid cell wall strengths similar to those of the fibre.

Acknowledgements. The views expressed in this paper are not endorsed by the National Science Foundation. The authors would like to thank Don Galler for training and assistance with the SEM, Alan Schwartzman for training and assistance with the Hysitron TriboIndenter, Mike Tarkanian, Ken Stone, Hayami Arakawa and Brian Chan for their help in the development specimen preparation methods. A special thanks goes to Greg Smith and Kate Semple at the University of British Columbia (Department of Wood Science), working on processing of SBP, Michael Ramage at Cambridge University (Department of Architecture), working on the structural performance of SBP, Helen Mulligan at Cambridge Architectural Research, working on thermal and moisture performance of SBP as well as life cycle assessment of SBP in buildings. Additional thanks to Kevin Chen and Marc Borrega at MIT (Department of Materials Science and Engineering) for their useful discussions about the work.

Data accessibility. Raw data will be made publically available through DSpace, the institute repository of Massachusetts Institute of Technology at http://dspace.mit.edu/handle/1721.1/88182.

Funding statement. This paper is based upon work supported by the National Science Foundation under OISE: 1258574.

References

1. Jiang Z. 2007 *Bamboo and rattan in the world*. Beijing, China: China Forestry Publishing House.
2. Harries KA, Sharma B, Richard M. 2012 Structural use of full culm bamboo: the path to standardization. *Int. J. Archit. Eng. Constr.* **1**, 66–75. (doi:10.7492/IJAEC.2012.008.)
3. Food and Agriculture Organization of the United Nations. 2010 *Global Forest Resource Assessment 2010*. Rome, Italy: Food and Agriculture Organization of the United Nations.
4. Fu J. 2000 Moso bamboo in China. *Am. Bamboo Soc. Mag.* **21**, 12–17.
5. Ding X, Cai H, Chen Y, Zhang J. 2007 Systematic analysis on the quick development of bamboo industry in Zhejiang province: a case study for successful development approach of China's booming bamboo industry. *Chin. For. Sci. Technol.* **6**, 74–82.
6. Grosser D, Liese W. 1971 On the anatomy of Asian bamboos, with special reference to their vascular bundles. *Wood Sci. Technol.* **5**, 290–312. (doi:10.1007/BF00365061)
7. Wegst UGK. 2011 Bending efficiency through property gradients in bamboo, palm, and wood-based composites. *J. Mech. Behav. Biomed. Mater.* **4**, 744–755. (doi:10.1016/j.jmbbm.2011.02.013)
8. Amada S, Ichikawa Y, Munekata T, Nagase Y, Shimizu H. 1997 Fiber texture and mechanical graded structure of bamboo. *Compos. Part B Eng.* **28B**, 13–20. (doi:10.1016/S1359-8368(96)00020-0)
9. Nogata F, Takahashi H. 1995 Intelligent functionally graded material: bamboo. *Compos. Eng.* **5**, 743–751. (doi:10.1016/0961-9526(95)00037-N)
10. Shao Z-P, Fang C-H, Huang S-X, Tian G-L. 2010 Tensile properties of Moso bamboo (*Phyllostachys pubescens*) and its components with respect to its fiber-reinforced composite structure. *Wood Sci. Technol.* **44**, 655–666. (doi:10.1007/s00226-009-0290-1)
11. Lee AWC, Bai X, Peralta PN. 1994 Selected physical and mechanical properties of giant timber bamboo grown in South Carolina. *For. Prod. J.* **44**, 40–46.
12. Janssen JJA. 1991 *Mechanical properties of bamboo*. Dordrecht, The Netherlands: Springer Science+Business Media.
13. Lo TY, Cui H, Leung H. 2004 The effect of fiber density on strength capacity of bamboo. *Mater. Lett.* **58**, 2595–2598. (doi:10.1016/j.matlet.2003.03.029)
14. Chung KF, Yu WK. 2002 Mechanical properties of structural bamboo for bamboo scaffoldings. *Eng. Struct.* **24**, 429–442. (doi:10.1016/S0141-0296(01)00110-9)
15. Yu Y, Fei B, Zhang B, Yu X. 2007 Cell-wall mechanical properties of bamboo investigated by *in-situ* imaging nanoindentation. *Wood Fiber Sci.* **39**, 527–535.
16. Wang Y, Leppänen K, Andersson S, Serimaa R, Ren H, Fei B. 2012 Studies on the nanostructure of the cell wall of bamboo using X-ray scattering. *Wood Sci. Technol.* **46**, 317–332. (doi:10.1007/s00226-011-0405-3)
17. Silva ECN, Walters MC, Paulino GH. 2006 Modeling bamboo as a functionally graded material: lessons for the analysis of affordable materials. *J. Mater. Sci.* **41**, 6991–7004. (doi:10.1007/s10853-006-0232-3)
18. Gibson LJ, Ashby MF. 1997 *Cellular solids: structure and properties*, 2nd edn. Cambridge, UK: Cambridge University Press.
19. Gibson LJ. 2012 The hierarchical structure and mechanics of plant materials. *J. R. Soc. Interface* **9**, 2749–2766. (doi:10.1098/rsif.2012.0341)
20. Kellogg RM, Wangaard FF. 1969 Variation in the cell-wall density of wood. *Wood Fiber Sci.* **1**, 180–204.
21. Oliver WC, Pharr GM. 1992 An improved technique for determining hardness and elastic modulus using load and displacement sensing indentation experiments. *J. Mater. Res.* **7**, 1564–1583. (doi:10.1557/JMR.1992.1564)
22. Eder M, Arnould O, Dunlop JWC, Hornatowska J, Salmén L. 2013 Experimental micromechanical characterisation of wood cell walls. *Wood Sci. Technol.* **47**, 163–182. (doi:10.1007/s00226-012-0515-6)
23. Gamstedt EK, Bader TK, Borst K. 2013 Mixed numerical–experimental methods in wood micromechanics. *Wood Sci. Technol.* **47**, 183–202. (doi:10.1007/s00226-012-0519-2)

24. Cave ID. 1968 The anisotropic elasticity of the plant cell wall. *Wood Sci. Technol.* **2**, 268–278. (doi:10.1007/BF00350273)
25. Andrews E, Sanders W, Gibson LJ. 1999 Compressive and tensile behaviour of aluminum foams. *Mater. Sci. Eng. A.* **270**, 113–124. (doi:10.1016/S0921-5093(99)00170-7)
26. Liese W, Schmitt U. 2006 Development and structure of the terminal layer in bamboo culms. *Wood Sci. Technol.* **40**, 4–15. (doi:10.1007/s00226-005-0046-5)
27. Hull D, Clyne TW. 1996 *An introduction to composites*, 2nd edn. Cambridge, UK: Cambridge University Press.
28. Jones RM. 1999 *Mechanics of composites materials*, 2nd edn. New York, NY: Taylor and Francis Group.
29. Collings TA. 1974 Transverse compressive behaviour of unidirectional carbon fibre reinforced plastics. *Composites* **5**, 108–116. (doi:10.1016/0010-4361(74)90548-5)
30. Li X. 2004 Physical, chemical, and mechanical properties of bamboo. MS thesis, Louisiana State University, Baton Rouge, LA, USA.
31. Forest Products Service. 2010 *Wood handbook*. Madison, WI: Forest Products Laboratory USDA.
32. Gerhards CC. 1982 Effect of moisture content and temperature on mechanical properties of wood: an analysis of immediate effects. *Wood Fiber* **14**, 4–36.
33. Mishnaevsky L, Qing H. 2008 Micromechanical modelling of mechanical behaviour and strength of wood: state-of-the-art review. *Comput. Mater. Sci.* **44**, 363–370. (doi:10.1016/j.commatsci.2008.03.043)
34. Wangaard FF. 1950 *The mechanical properties of wood*. New York, NY: John Wiley and Sons, Inc.
35. ASTM Standard D143, 2009. 2009 *Standard test methods for small clear specimens of timber*. West Conshohocken, PA: ASTM International.